Atmos. Meas. Tech. Discuss., 5, 7729–7752, 2012
www.atmos-meas-tech-discuss.net/5/7729/2012/
doi:10.5194/amtd-5-7729-2012

Atmospheric Measurement Techniques Discussions

Thermodynamic phase retrieval of convective clouds: impact of sensor viewing geometry and vertical distribution of cloud properties

E. Jäkel, J. Walter, and M. Wendisch

Leipzig Institute for Meteorology (LIM), University of Leipzig, Germany

Received: 14 September 2012 – Accepted: 8 October 2012 – Published: 22 October 2012

Correspondence to: E. Jäkel (e.jaekel@uni-leipzig.de)

Published by Copernicus Publications on behalf of the European Geosciences Union.

Abstract

The potential to use combined passive and active remote sensing measurements to retrieve microphysical parameters of convective clouds in particular thermodynamic phase, is investigated by three-dimensional (3-D) radiative transfer simulations. The 3-D simulations are used to quantify the effect of different viewing geometries and distributions of the cloud microphysical properties on the derived ice index. Measurement examples of spectral solar and radiance reflected by cloud sides (passive) in the near-infrared (NIR) spectral range are synchronized with collocated Lidar observations (active). A retrieval method to distinguish the cloud thermodynamic phase (liquid water or ice) using the reported reflectivity measurements is applied which uses the different spectral slopes of water and ice clouds in the NIR. The concurrent depolarization backscattering Lidar provides geometry information about the cloud distance and height as well as the depolarization.

1 Introduction

Clouds are relevant components of the Earth's climate (IPCC, 2007). Depending on the cloud properties (top and bottom height, thermodynamic phase, optical thickness, and droplet or particle size), they have the potential to either cool or warm the atmosphere beneath the cloud. Different processes may influence the coagulation (collision and coalescence) and freezing mechanisms inside clouds which determine the precipitation formation, the lifetime and vertical extent of the cloud (Rosenfeld, 2000; Koren et al., 2004; Lohmann and Feichter, 2005; Khain et al., 2008). Rosenfeld and Lensky (1998) found that the relation between temperature or height and cloud particle effective radius provides significant information on precipitation-forming processes in convective clouds. To investigate these complex interactions vertical profile measurements on microphysical (such as thermodynamic phase, cloud particle size and liquid or ice water content) and radiative properties are essential.

Discussion Paper | Discussion Paper | Discussion Paper | Discussion Paper |

AMTD

5, 7729–7752, 2012

Traditionally, vertical profiling of clouds is mostly based on Radar and Lidar or in situ measurements. Radar and Lidar are not always available on aircraft. The sample volume of in situ measurements is restricted to the flight path of the aircraft. Also, characterizing the vertical structure of a cloud is biased by the temporal evolution of the cloud while the aircraft is climbing from cloud base to cloud top. For deep convective clouds strong turbulence complicates in situ probing.

Active remote sensing provides profiles along the line-of-sight, depending on the penetration depth of the radiation source (either coherent monochromatic electromagnetic waves in case of Lidar or radio waves for Radar). In general, Lidar does not penetrate deeply into the cloud (up to an optical depth of 2–4), but it provides detailed information about the optical properties of the cloud edges. Radar may penetrate through a cloud but the quantitative retrieval of cloud optical and microphysical properties is uncertain since the signal is dominated by scattering by large droplets. Lidar measurements of the degree of linear polarization can be used to determine the thermodynamic phase (Scotland et al., 1971; Sassen, 1991). The quantity to describe the degree of linear depolarization is the linear depolarization ratio δ which is the ratio of the perpendicular and parallel polarized backscattered intensities with respect to the transmitter polarization plane. Non-spherical particles such as ice crystals may rotate the oscillation plane of the electric and magnetic field vectors, thus causing significant depolarization. Since multiple scattering also increases the depolarization ratio of liquid water clouds with increasing penetration depth, the change of δ with depth has to be examined which contains the information about the thermodynamic phase (Hu et al., 2001).

Spaceborne and airborne passive remote sensing methods are based on measuring the reflected solar and emitted terrestrial radiances. Such observations have successfully been applied to retrieve the cloud macro- and microphysical-structure. The retrieval of vertical profiles from nadir or zenith radiance observations is inherently limited to determine either bulk properties integrated over the entire column (like the optical thickness) or to quantities representative of cloud top (like the thermodynamic phase

AMTD
5, 7729–7752, 2012

or droplet size). However, vertical information cannot be derived by these instruments. Current satellite and aircraft retrieval methods are mostly based on one-dimensional (1-D) radiative transfer simulations which assume that clouds are horizontally homogeneous. While such an approach might be feasible for a cloud-top-viewing instrument, for the proposed cloud-side-scanning geometry the consideration of 3-D effects is mandatory. Zinner et al. (2008) and Martins et al. (2011) presented an airborne cloud scanner that measures spectral radiances reflected from cloud sides which potentially allows the retrieval of the vertical profile of cloud droplet sizes near cloud edges. Under certain assumptions this vertical distribution corresponds to the vertical profile of the whole cloud (Rosenfeld and Lensky, 1998; Freud et al., 2008).

Retrieving the effective radius requires knowledge about the thermodynamic phase, because the optical properties of ice and liquid water clouds deviate significantly. The retrieval of the thermodynamic phase is often based on two methods, one using the different emissivity of ice and liquid water particles in the thermal infrared (TIR: 5–50 µm) wavelength range (Strabala and Ackerman, 1994; Baum et al., 2000; Turner et al., 2003); the other approach applies cloud reflectivity measurements in the near infrared (NIR: 0.7–2.5 µm), where the refractive indices of the cloud particles of both phases are different (Pilewskie and Twomey, 1987; Knap et al., 2002; Acarreta et al., 2004; Ehrlich et al., 2008). Exemplarily, the imaginary part of the refractive index determining the absorption of electromagnetic radiation due to ice is larger than for liquid water in the wavelength range between 1.5–1.7 µm. Therefore, the ratio of cloud reflectances at two wavelengths can be used to determine the cloud thermodynamic phase. For satellite-based data of the Scanning Imaging Absorption Spectrometer for Atmospheric CHartographY (SCIAMACHY) Acarreta et al. (2004) used this ratio-method and defined a cloud phase index which is calculated by fitting the spectral slope of the reflectivity around 1.6 µm and it's normalization with the reflectivity at 1.64 µm. Knap et al. (2002) and Ehrlich et al. (2008) applied the ratio-method based on airborne measurements of nadir reflectances while Martins et al. (2011) used reflectivity at 2.10 µm and 2.25 µm from cloud sides. Ground-based measurements of cloud side reflectivity were

AMTD
5, 7729–7752, 2012
Thermodynamic phase retrieval of convective clouds
E. Jäkel et al.

performed by Pilewskie and Twomey (1987). They used normalized spectra between 1.5 to 1.7 µm to derive the cloud phase.

Compared to previous publications by Martins et al. (2011) and Pilewskie and Twomey (1987) this paper introduces an extension of the known ground-based passive remote sensing with additional active remote sensing of the cloud thermodynamic phase for side viewing geometries. The retrieval method is systematically investigated with respect to viewing geometry and vertical distribution of cloud properties by 3-D radiative transfer simulations. The spectral signature between 1.5–1.7 µm of the reflected radiation is used to identify the cloud phase. Additionally, collocated Lidar data give important information about the viewing geometry. It is shown, if there is a threshold which defines liquid, ice and mixed cloud phase. Section 2 describes the 3-D radiative transfer model (RTM) and the instrumentation used in this work. In Sect. 3 sensitivity studies of the derived cloud phase with respect to cloud microphysics and viewing geometry based on RTM results are presented. Finally, the application of the phase discrimination method is examined by a case study of observations in Sect. 4.

2 Methods and materials

2.1 Modeling

Radiative transfer simulations are performed with the open-source Monte Carlo Atmospheric Radiative Transfer Simulator (MCARATS), which is a forward-propagating Monte Carlo photon-transport model (Iwabuchi, 2006; Iwabuchi and Kobayashi, 2008). It traces individual photons on their path through the 3-D atmosphere. Input to the radiative transfer model (RTM) are the optical properties of the atmosphere (e.g. extinction coefficients, single scattering albedos, phase functions) and the surfaces albedo. The model domain is divided into grid cells. The user is enabled to specify 3-D layers for horizontal inhomogeneous distributions of cloud or aerosol particles. Other layers can be defined as horizontally homogeneous, as applied for the optical properties of gaseous

AMTD
5, 7729–7752, 2012

constituents. Profiles of atmospheric pressure, temperature, density, and gases are taken from profiles given by Anderson et al. (1986). Molecular (Rayleigh) scattering is calculated from the density profile according to Bodhaine et al. (1999). For gas absorption the LOWTRAN (Low Resolution Transmission Model) parametrization by Pierluissi and Peng (1985), as adapted from SBDART (Santa Barbara DISORT Atmospheric Radiative Transfer) (Ricchiazzi and Gautier, 1998) are used. The optical properties of liquid water and ice clouds with profiles of effective radius (r_{eff}) and liquid (ice) water content (LWC, IWC) are specified in 3-D layers. The microphysical properties of water clouds are converted to optical properties by Mie calculations, while for ice clouds the parameterizations by Baum et al. (2005, 2007) are applied. Further input variables are the extraterrestrial spectrum as taken from Gueymard (2004) and the solar zenith and azimuth angles (θ_0, φ_0) as well as sensor zenith and azimuth angles (θ_s, φ_s).

2.2 Instrumentation

Lidar and spectroradiometer measurements are performed by the Lidar and RAdiation System for cloud profiling (LIRAS). The instrument setup is schematically shown in Fig. 1. Lidar and optical inlet of the spectroradiometer are mounted on a joint angular tracker with an angular resolution of about 1° to scan cloud sides simultaneously with passive and active sensors. The field of view (FOV) of the radiance optical inlet is about 1°, and thus larger than that of the Lidar (0.114°), which results in a different footprint diameter. Exemplarily, for a cloud distance of 10 km the footprints are about 170 m (radiance inlet) and 20 m (Lidar), respectively.

The spectroradiometer is a ground-based version of the airborne SMART (Spectral Modular Airborne radiation measurement system). It provides measurements of radiances covering almost the entire solar spectral range (Wendisch et al., 2001; Bierwirth et al., 2009; Jäkel et al., 2005; Ehrlich, 2009). The radiation is collected by an entrance optics and transmitted via bifurcated optical fiber to two spectrometers; one for the visible (VIS) spectral range, the other for the NIR. Within the spectrometers a fixed-grating disperses the radiation into spectral components which are detected by

AMTD
5, 7729–7752, 2012

photodiodes. The measurement uncertainty of the spectroradiometer includes calibration lamp and transfer calibration uncertainties (between laboratory and field) as well as the wavelength accuracy of the spectrometers. That gives total relative uncertainties in the visible spectral range of 6 % and 9 % for the NIR (Eichler et al., 2009).

For this application an ice index I_s is defined from the spectral slope of the radiance at 1550 nm I_{1550} and 1700 nm I_{1700}, respectively:

$$I_s = \frac{I_{1550} - I_{1700}}{I_{1700}}. \quad (1)$$

The definition of this index is based on differences in spectral shapes of reflected radiances as presented in Fig. 2 which shows examples of measured NIR radiance spectra of ice and liquid water clouds reflected from cloud sides. The spectral signature of radiance cloud spectra is mainly different within the range between 1.5 and 1.7 µm. In this case, the slope is positive for ice clouds and negative for liquid water clouds. In Sect. 3 it will be shown by radiative transfer simulation, if this is a general characteristic for variable viewing geometries and cloud properties.

The depolarization backscattering Lidar system (ALS300 from Leosphere, France) is primarily used for geometric information on the observed cloud. In addition, the slope of the depolarization can give an indication on the thermodynamic phase. Table 1 summarizes the technical specifications of LIRAS.

3 Sensitivity study

3.1 Homogeneous cloud

3-D radiative transfer simulations of reflected radiances on cloud sides are performed for different sensor viewing geometries. From these calculations at 1.55 µm and 1.7 µm wavelength the ice index I_s was derived using Eq. (1). The model domain has $140 \times 40 \times 139$ grid cells with a horizontal resolution grid cell of 250 m and a vertical resolution of

AMTD
5, 7729–7752, 2012

200 m below 22 km and variable resolution above. A homogeneous cloud (15 × 40 × 16 grid cells) either consisting of liquid water droplets or of ice crystals is placed into the center of the model domain between 3.8 and 7.0 km altitude. MCARATS simulates radiances for all 140 × 40 grid points at surface altitude. In a first step the ice index I_s is determined for a solar azimuth angle $\varphi_0 = 0°$, a solar zenith angle $\theta_0 = 30°$ and variable sensor azimuth and zenith angles (φ_s, θ_s) between 0 and 80° in steps of 10°. The effective radius r_{eff} of the ice and the liquid water cloud is fixed to 15 µm.

Figure 3 shows the relative frequency of the ice indices of both clouds for all points in the model domain from which the reflected radiation of the cloud side are simulated. Overall, there is clear separation between liquid water clouds and ice clouds. Positive values of I_s corresponds to ice clouds and negative values indicate a liquid water cloud element. The large range of ice index values indicates a significant impact of the sensor geometry which is illustrated in Fig. 4a. It presents the derived ice indices for clouds with uniform r_{eff} and thermodynamic phase. Here, sensor and solar azimuth angle are fixed to 0° which means that the sun is in the back of the observer. For this configuration the sensor zenith angle θ_s was varied between 20° and 80° in 2° steps. As shown in Fig. 4 the viewing geometry in terms of the scattering angle affects I_s significantly. In this case, an increase of the sensor zenith angle and so the scattering angles (ranging here between 50 and 115°) results in an increase of the ice index I_s for ice and liquid water clouds. This geometry effect can be also observed for varying the sensor azimuth angle (Fig. 4b) for a fixed the sensor zenith angle. In Fig. 4b I_s is shown for ice and liquid water clouds with r_{eff} = 15 µm and a fixed sensor zenith angle of $\theta_s = 70°$. Again, the sign of the ice index clearly separates the two thermodynamic phases in spite of the varying sensor viewing geometry. Additionally, Fig. 4a shows the dependence of the ice index I_s from the cloud particle size and phase. The ice index of liquid water independent on particle size is mostly lower than zero, whereas ice clouds show a positive ice index. Due to the increasing absorption the largest ice index is derived for ice particles with r_{eff} = 50 µm. Less absorbing particles lead to lower values of I_s.

AMTD
5, 7729–7752, 2012

Summarizing, even clouds with uniform microphysical parameters can yield a variety of ice indices, depending on the viewing geometry. Nevertheless, the thermodynamic phase can clearly be distinguished by the sign of I_s.

The simulations are performed with a LWC/IWC of 0.7 g m^{-3}. Additionally, the water content is varied to estimate the impact of that parameter on the ice index. The viewing geometry is fixed ($\theta_s = 50^\circ$, $\theta_0 = 30^\circ$, $\varphi_s = \varphi_0 = 0^\circ$), while the ice index is simulated for ice and liquid clouds with different effective radii. In all cases shown in Fig. 5 the ice index is mostly variable for water content values below 0.4 g m^{-3} (above 20 %). Above that threshold the variation of I_s is below 7 %. However, for the remote sensing of the thermodynamic phase the liquid or ice water content is not a critical parameter which needs to be known.

3.2 Vertically inhomogeneous clouds

In a next step, the effective radius and LWC/IWC are varied in vertical direction. Horizontally the cloud is assumed as homogeneous. The vertical extension of the cloud is between 3.8 to 13 km, consisting of ice in the upper part (7.0–13.0 km) and liquid water in the lower part (3.8–6.4 km). In between there is a mixed phase layer (6.4–7.0 km) (see Fig. 6a). Fig. 6b shows the profile of the single scattering albedo $\tilde{\omega}$ of the individual cloud particles. Due to the wide range of effective radii (7–44 µm) $\tilde{\omega}$ of ice particles varies much stronger (0.88–0.98 for 1550 nm wavelength) than $\tilde{\omega}$ of the liquid water particles, which is about 0.99. The profile of the ice index was derived for the side viewing geometry with: $\varphi_s = \varphi_0 = 0^\circ$, $\theta_0 = 30^\circ$ and a range of θ_s between 20 and 80°. For a distance to the cloud of about 9 km (corresponds to $36^\circ < \theta_s < 66^\circ$) the profile of the derived ice index is shown in Fig. 6c. It illustrates a clear separation of ice and liquid phase. Also the mixed phase layer can be identified. However, in the most upper part of the cloud with ice particles of $r_{\mathrm{eff}} < 20$ µm the ice index could be misinterpreted as liquid particles because of their high $\tilde{\omega}$ (> 0.98). In addition to the variable LWC/IWC (filled squares in Fig. 6c) also simulations with fixed water content (0.7 g m^{-3}) are performed. Their difference is largest in the mixed-phase layer and at the top of the cloud where the variable IWC is much lower than $0.7\,g\,m^{-3}$. While the ice index of liquid water layer is less sensitive to the variability of LWC-values due to high $\tilde{\omega}$, the differences of the ice index for the ice layer depends strongly on the effective radius. Large effective radius (as at the bottom of the layer) results in a strong absorption which is increased for larger a IWC. Therefore, the ice index for $IWC = 0.7\,g\,m^{-3}$ is larger than for the IWC of $0.2\,g\,m^{-3}$ at 6.4 km altitude which is in contrast to the cloud top. There the small ice particles lead to a decrease of the ice index with increasing IWC. However, for most part of the I_s-profile the fixed and the variable water content give similar values. From the above it can be concluded that the sensitivity of the ice index with regard to the water content is negligible for threshold value which depends on the cloud particle size and thermodynamic phase.

4 Measurement example

Observations of convective clouds passing Leipzig, Germany, were performed on 25 June 2012. Due to the high velocity of the passing clouds and their low horizontal extension time series at constant observation angle of the radiance were taken instead of full vertical profiles. Some of the clouds included precipitation, an indication for the existence of ice phase in the cloud. Satellite-based measurements with MODIS (Moderate-resolution Imaging Spectroradiometer) classified the cloud tops of the cloud field as ice and mixed-phase.

The time series of the reflected radiance at 1550 nm wavelength indicates the strong variability of the cloud situation (black line in Fig. 7). The data interpretation is supported by photos which help to identify cloud shadows. These spectral radiance data from shadowed clouds cannot be used for phase discrimination, because the origin of the multi-scattered radiance is unknown. However, also the absolute value of the radiance is a good indicator of possible shadow effects. In Fig. 7 four points of the time series are highlighted. At time step 1, 2 and 4 the radiance is about $0.02\,W\,m^{-2}\,nm^{-1}\,sr^{-1}$, but the corresponding ice index varies between −0.17 (liquid water phase) and +0.33

AMTD
5, 7729–7752, 2012
Thermodynamic phase retrieval of convective clouds
E. Jäkel et al.

(ice phase). Also the mixed phase can be identified at time step 1 with $I_s \approx 0$. Even lower ice index values of up to −0.8 were observed shortly after the mixed-phase cloud. In this case the ice index is misleading, because no cloud side reflection is measured. This low ice index results from either clear sky measurements or shadow effects which can be derived from the absolute radiance and LIDAR data. In contrast, time step 3 shows an ice index of about 0.7 which is much larger than derived for the results of the sensitivity studies. At this time step we had an overcast situation with a large precipitating convective cloud passing the measurement site, which is also denoted by the low radiance values. However, the high ice index indicates a large ice fraction in the passing cloud which affect the measured spectrum.

In addition to the measured ice indices at time step 1, 2 and 3 also the slope of the depolarization δ was determined from the Lidar measurements. In general the δ-slope of liquid water clouds is one order of magnitude lower than for ice clouds, which was also found for the time step 2 and 4.

Based on the given geometry ($\theta_0 = 30^\circ$, $\theta_s = 65^\circ$, and $\varphi_0 - \varphi_s = 60^\circ$) the particle size was varied to simulate an ice index close to the measured result (Table 2). For time step 2 an effective radius of 35 µm an ice index of +0.31 (measurement: +0.33) was simulated, while for the liquid water cloud a r_{eff} of 10 µm gave an ice index of −0.14 (measurement: −0.17).

5 Conclusions

Ground-based measurements of spectral radiances reflected from convective cloud edges were used to identify the thermodynamic phase of the cloud, which is needed for the retrieval of the effective radius. For that purpose an ice index was introduced which considers the different spectral slopes for ice and liquid water clouds between 1.55 µm and 1.7 µm. The slope difference results from deviations of the refraction index for ice and liquid water in this spectral range. Sensitivity studies performed with a 3-D radiative transfer model have shown that the ice index is quite sensitive to the effective radius and

AMTD
5, 7729–7752, 2012

the viewing geometry. Simulations of homogeneous clouds with constant microphysical properties illustrates that different viewing geometries lead to differences in the ice index which strongly depend on the range of scattering angles. However, in most of the cases the sign of the ice index was a clear indicator of the thermodynamic phase when dealing with pure liquid water or pure ice clouds. For clouds with mixed-phase layers the general statement, that a negative slope of the ice index corresponds to liquid water clouds and a positive slope indicates an ice cloud is not solid. The second sensitivity study investigated the profile of a complex cloud with ice, liquid water and mixed phase layers and variable effective radii and water content. From the ice index profile we could clearly identify all three layers, which gives confidence that detailed profile measurements of complex clouds can deliver cloud phase information, even for the critical mixed phase. Limitations of this method are given by the cloud and viewing geometry. Shadow effects which can be omitted by an observing geometry with the sun in the back of the observer, must be omitted. They lead to a misinterpretation of the ice index.

A case study of measured ice indices for passing convective clouds has shown signature of all three phases which was also found by depolarization measurements of the Lidar (slope of depolarization between 0.005 for liquid water and 0.02 for ice phase). From the measured ice index and the given viewing geometry the particle size was estimated with r_{eff} of 35 µm and 10 µm for the ice and liquid water cloud, respectively. We can conclude for this kind of measurements which investigated fast moving clouds, that a direct comparison with Lidar data is difficult due to its large accumulation time. But for viewing geometry purposes (sensor distance to the cloud) the Lidar system is essential.

Acknowledgements. This research was funded by the German Research Foundation (DFG, JA 2023/2-1). We thank Sebastian Schmidt and Shi Song from the University of Colorado, Boulder, for their help with the radiative transfer model MCARATS.

AMTD
5, 7729–7752, 2012

References

Acarreta, J. R., Stammes, P., and Knap, W. H.: First retrieval of cloud phase from SCIAMACHY spectra around 1.6 µm, Atmos. Res., 72, 89–105, doi:10.1016/j.atmosres.2004.03.027, 2004. 7732

Anderson, G., Clough, S., Kneizys, F., Chetwynd, J., and Shettle, E.: AFGL Atmospheric Constituent Profiles (0–120 km), Tech. Rep. AFGL-TR-86-0110, AFGL (OPI), Hanscom AFB, MA 01736, Air Force Geophys. Lab., Hanscom Air Force Base, Bedford, Mass., USA, 1986. 7734

Baum, B. A., Soulen, P., Strabala, K., King, M., Ackerman, S., Menzel, W., and Yang, P.: Remote sensing of cloud properties using MODIS airborne simulator imagery during SUCCESS, 2. Cloud thermodynamic phase, J. Geophys. Res., 105, 11781–11792, 2000. 7732

Baum, B. A., Heymsfield, A. J., Yang, P., and Bedka, S. T.: Bulk scattering properties for the remote sensing of ice clouds, Part 1: Microphysical data and models, J. Appl. Meteor., 44, 1885–1895, 2005. 7734

Baum, B. A., Yang, P., Nasiri, S., Heidinger, A., Heymsfield, A., and Li, J.: Bulk scattering properties for the remote sensing of ice clouds, Part 3: High resolution spectral models from 100 to 3250 cm^{-1}, J. Appl. Meteor., 46, 423–434, 2007. 7734

Bierwirth, E., Wendisch, M., Ehrlich, A., Heese, B., Tesche, M., Althausen, D., Schladitz, A., Müller, D., Otto, S., Trautmann, T., Dinter, T., von Hoyningen-Huene, W., and Kahn, R.: Spectral surface albedo over Morocco and its impact on the radiative forcing of Saharan dust, Tellus, 61B, 252–269, 2009. 7734

Bodhaine, B., Wood, N., Dutton, E., and Slusser, J.: On Rayleigh oprical depth calculations, J. Atmos. Ocean. Technol., 16, 1854–1861, 1999. 7734

Ehrlich, A.: The Impact of Ice Crystals on Radiative Forcing and Remote Sensing of Arctic Boundary-Layer Mixed-Phase Clouds, Ph. D. thesis, Johannes Gutenberg University, Mainz, Germany, 2009. 7734

Ehrlich, A., Wendisch, M., Bierwirth, E., Herber, A., and Schwarzenböck, A.: Ice crystal shape effects on solar radiative properties of Arctic mixed-phase clouds – Dependence on microphysical properties, Atmos. Res., 88, 266–276, 2008. 7732

Eichler, H., Ehrlich, A., Wendisch, M., Mioche, G., Gayet, J.-F., Wirth, M., Emde, C., and Minikin, A.: Influence of ice crystal shape on retrieval of cirrus optical thickness and effective radius: a case study, J. Geophys. Res., 114, D19203, doi:10.1029/2009JD012215, 2009. 7735

AMTD
5, 7729–7752, 2012

Thermodynamic phase retrieval of convective clouds

E. Jäkel et al.

Title Page
Abstract | Introduction
Conclusions | References
Tables | Figures
◀I | ▶I
◀ | ▶
Back | Close
Full Screen / Esc
Printer-friendly Version
Interactive Discussion

Freud, E., Rosenfeld, D., Andreae, M. O., Costa, A. A., and Artaxo, P.: Robust relations between CCN and the vertical evolution of cloud drop size distribution in deep convective clouds, Atmos. Chem. Phys., 8, 1661–1675, doi:10.5194/acp-8-1661-2008, 2008. 7732

Hu, Y.-X., Winker, D., Yang, P., Baum, B., Poole, L., and Vann, L.: Identification of cloud phase from PICASSO-CENA lidar depolarization: a multiple scattering sensitivity study, J. Quant. Spectrosc. Ra., 70, 569–579, 2001. 7731

IPCC: Climate Change 2007: the Physical Science Basis, Cambridge University Press, Cambridge, UK, 2007. 7730

Iwabuchi, H.: Efficient Monte Carlo methods for radiative transfer modeling, J. Atmos. Sci., 63, 2324–2339, 2006. 7733

Iwabuchi, H. and Kobayashi, H.: Modeling of radiative transfer in cloudy atmospheres and plant canopies using Monte Carlo methods, Tech. rep., FRCGC, No.8, 199 pp., Frontier Research Center for Global Change (FRCGC), Japan Agency for Marine-Earth Science and Technology (JAMSTEC), Japan, 2008. 7733

Jäkel, E., Wendisch, M., Kniffka, A., and Trautmann, T.: Airborne system for fast measurements of upwelling and downwelling spectral actinic flux densities, Appl. Optics, 44, 434–444, 2005. 7734

Khain, A., BenMoshe, N., and Pokrovsky, A.: Factors determining the impact of aerosols on surface precipitation from clouds: attempt of classification, J. Atmos. Sci., 65, 1721–1748, 2008. 7730

Knap, W., Stammes, P., and Koelemeijer, R.: Cloud thermodynamic-phase determination from near-infrared spectra of reflected sunlight, J. Atmos. Sci., 59, 83–96, 2002. 7732

Koren, I., Kaufman, Y., Remer, L., and Martins, J.: Measurement of the effect of amazon smoke on inhibition of cloud formation, Science, 303, 1342–1345, 2004. 7730

Lohmann, U. and Feichter, J.: Global indirect aerosol effects: a review, Atmos. Chem. Phys., 5, 715–737, doi:10.5194/acp-5-715-2005, 2005. 7730

Martins, J. V., Marshak, A., Remer, L. A., Rosenfeld, D., Kaufman, Y. J., Fernandez-Borda, R., Koren, I., Correia, A. L., Zubko, V., and Artaxo, P.: Remote sensing the vertical profile of cloud droplet effective radius, thermodynamic phase, and temperature, Atmos. Chem. Phys., 11, 9485–9501, doi:10.5194/acp-11-9485-2011, 2011. 7732, 7733

Pierluissi, J. and Peng, G.-S.: New molecular transmission band models for LOWTRAN, Opt. Eng., 24, 541–547, 1985. 7734

AMTD
5, 7729–7752, 2012

Thermodynamic phase retrieval of convective clouds

E. Jäkel et al.

Pilewskie, P. and Twomey, S.: Discrimination of ice from water in clouds by optical remote sensing, Atmos. Res., 21, 113–122, 1987. 7732, 7733
Ricchiazzi, P. and Gautier, C.: Investigation of the effect of surface heterogeneity and topography on the radiation environment of Palmer Station, Antarctica, with a hybrid 3-D radiative transfer model, J. Geophys. Res., 103, 6161–6178, 1998. 7734
Rosenfeld, D.: Suppression of rain and snow by urban and industrial air pollution, Science, 287, 1793–1796, 2000. 7730
Rosenfeld, D. and Lensky, I.: Satellite-based insights into precipitation formation processes in continental and maritime convective clouds, Bull. Am. Meteorol. Soc., 79, 2457–2476, 1998. 7730, 7732
Sassen, K.: The polarization lidar technique for cloud research: a review and current assessment, Bull. Am. Meteorol. Soc., 72, 1848–1866, 1991. 7731
Scotland, R. M., Sassen, K., and Stone, R.: Observations by lidar of linear depolarizations of hydrometeors, J. Appl. Meteor., 10, 1011–1017, 1971. 7731
Strabala, K. and Ackerman, S.: Cloud properties from 8–12 µm data, J. Appl. Meteorol., 33, 212–229, 1994. 7732
Turner, D. D., Ackerman, S. A., Baum, B. A., Revercomb, H. E., and Yang, P.: Cloud phase determination using ground-based AERI observations at SHEBA, J. Appl. Meteor., 42, 701–715, 2003. 7732
Wendisch, M., Müller, D., Schell, D., and Heintzenberg, J.: An airborne spectral albedometer with active horizontal stabilization, J. Atmos. Ocean. Technol., 18, 1856–1866, 2001. 7734
Zinner, T., Marshak, A., Lang, S., Martins, J. V., and Mayer, B.: Remote sensing of cloud sides of deep convection: towards a three-dimensional retrieval of cloud particle size profiles, Atmos. Chem. Phys., 8, 4741–4757, doi:10.5194/acp-8-4741-2008, 2008. 7732

Table 1. Technical Specifications of LIRAS. FWHM: Full Width at Half Maximum.

	Zeiss Spectrometer	Lidar (Leosphere ALS300)
Wavelength (nm)	350–2000	355
Spectral Resolution (nm)	$FWHM_{VIS} = 3$ $FWHM_{NIR} = 16$ $\Delta\lambda_{VIS} = 0.8$ $\Delta\lambda_{NIR} = 5$	–
Accumulation Time (s)	1	10–30
Field of View (°)	1	0.114
Polarization	–	Vertical and Parallel

AMTD
5, 7729–7752, 2012

AMTD
5, 7729–7752, 2012

Table 2. Comparison of ice indices and Lidar depolarization slopes.

	Mixed Phase (1)	Ice Phase (2)	Liquid Phase (4)
Lidar δ-slope	0.01	0.02	0.005
Measured Ice Index I_s	0.02	0.33	−0.17
Simulated Ice Index I_s	–	0.31[a]	−0.14[b]

[a] $r_{\mathrm{eff}} = 35\,\mu\mathrm{m}$;
[b] $r_{\mathrm{eff}} = 10\,\mu\mathrm{m}$.

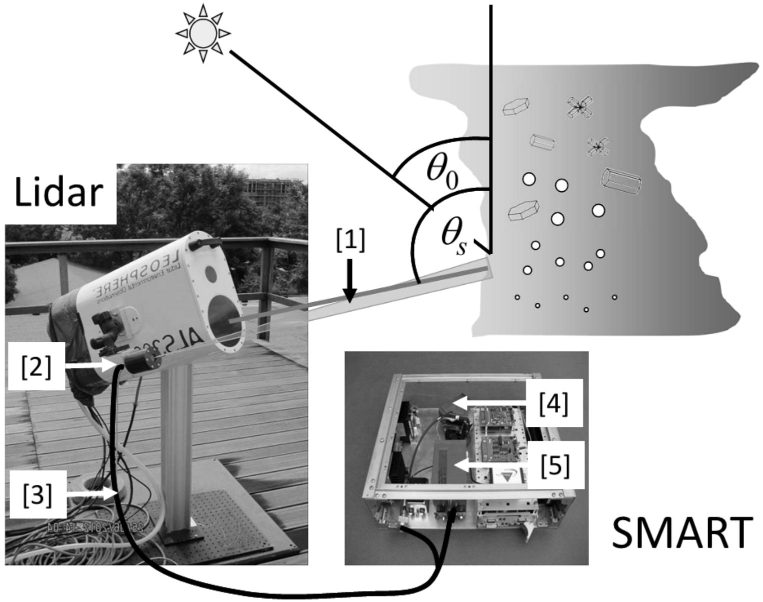

Fig. 1. LIRAS setup consisting of depolarization Lidar and SMART-spectroradiometer. (1) Schematic field of view (FOV) of both instruments, (2) radiance optical inlet, (3) optical fiber, (4) NIR spectrometer, and (5) VIS spectrometer. Additionally, the sensor and solar zenith angle (θ_s, θ_0) are illustrated.

AMTD
5, 7729–7752, 2012

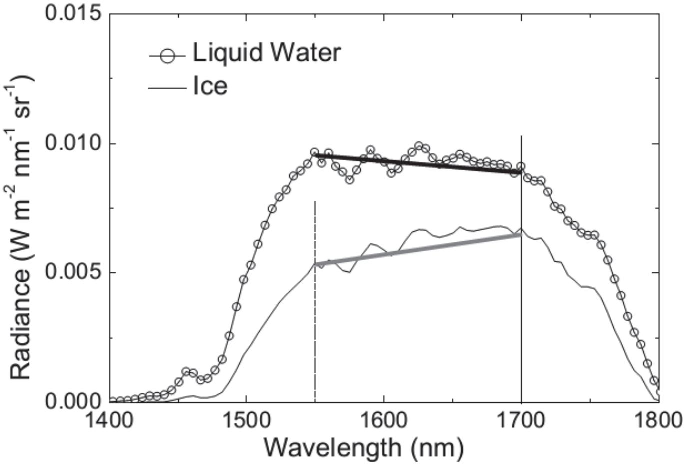

Fig. 2. Measured spectral radiance of cloud edges with ice cloud and liquid water cloud particles.

AMTD
5, 7729–7752, 2012

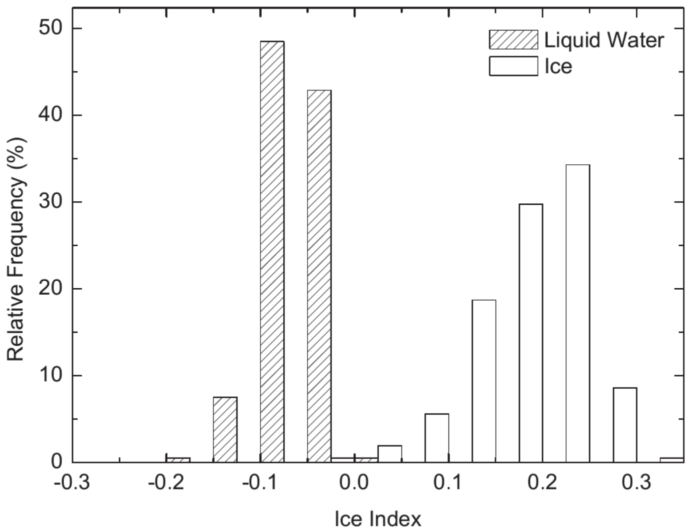

Fig. 3. Relative frequency of ice indices for ice and liquid water clouds (r_{eff} = 15 µm) for varied sensor viewing geometries based on 600 cases.

AMTD
5, 7729–7752, 2012

Thermodynamic phase retrieval of convective clouds

E. Jäkel et al.

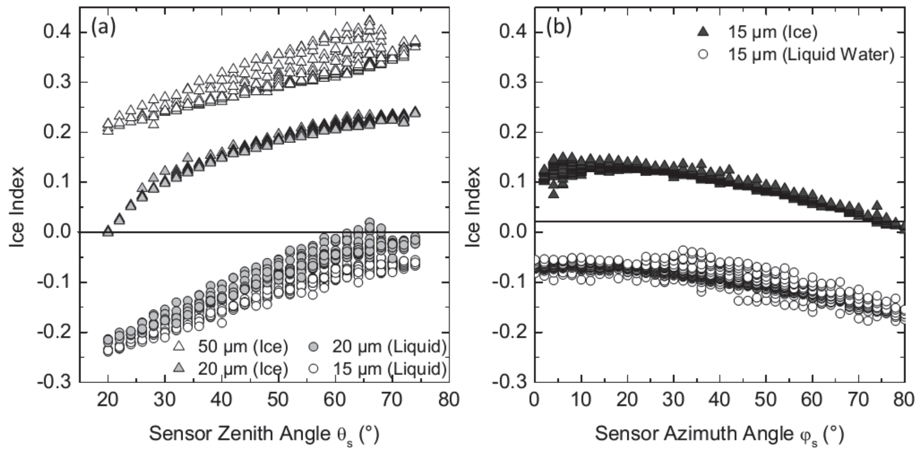

Fig. 4. (a) Ice index derived of water and ice clouds with r_{eff} = 15 µm and varied sensor zenith angles. **(b)** Same as **(a)** but for varied sensor azimuth angle.

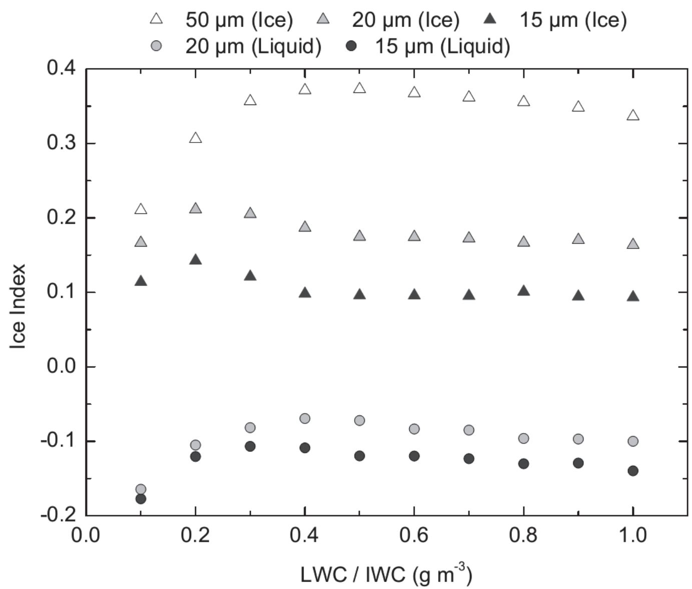

Fig. 5. Ice index dependence on LWC and IWC, respectively for fixed viewing geometry (θ_s = 50°, φ_s = 0°).

AMTD
5, 7729–7752, 2012

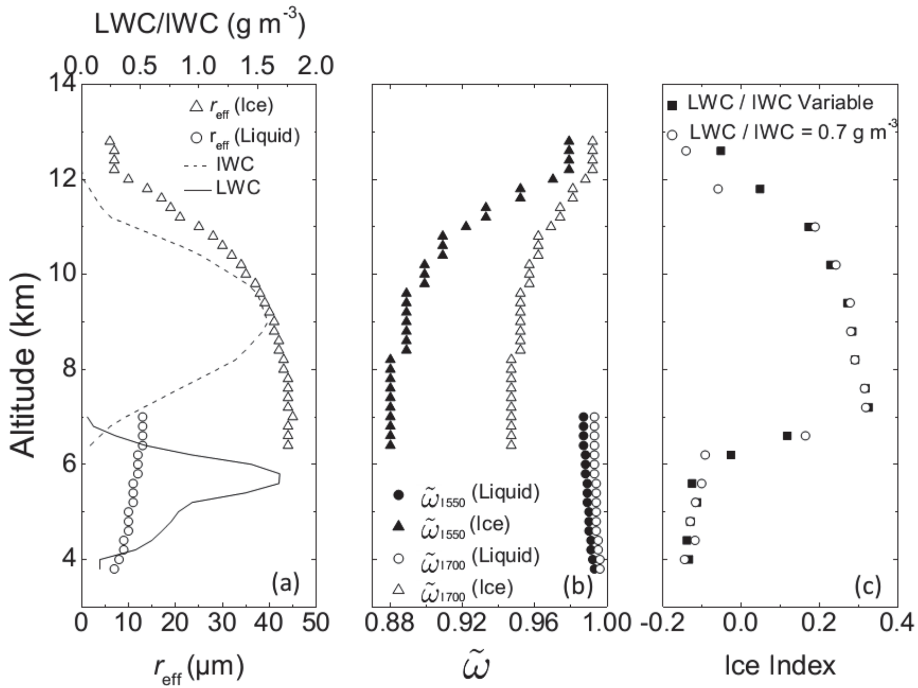

Fig. 6. (a) Vertical profile of r_{eff} and water contents. **(b)** Single scattering albedo $\tilde{\omega}$ as derived from Mie-calculation for liquid water and taken from the Baum parametrization for ice particles, and **(c)** ice index profile.

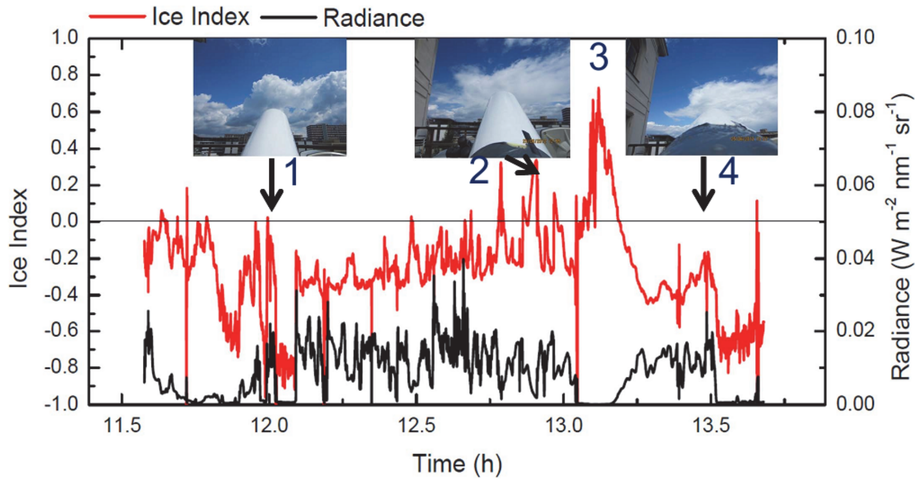

Fig. 7. Time series of spectral radiance at 1550 nm wavelength (black) and derived ice index (red).

AMTD
5, 7729–7752, 2012